

Coupling of Surface-Plasmon-Polariton-Hybridized Cavity Modes between Submicron Slits in a Thin Gold Film

Roman Walther,^{*,†} Stefan Fritz,[†] Erich Müller,[†] Reinhard Schneider,[†] Dagmar Gerthsen,[†] Wilfried Sigle,[‡] Tsofar Maniv,[§] Hagai Cohen,^{||} Christian Matyssek,[⊥] and Kurt Busch^{⊥,#}

[†]Laboratorium für Elektronenmikroskopie, Karlsruher Institut für Technologie (KIT), 76128 Karlsruhe, Germany

[‡]Max-Planck-Institut für Festkörperforschung, 70569 Stuttgart, Germany

[§]Schulich Faculty of Chemistry, Technion – Israel Institute of Technology, Haifa 32000, Israel

^{||}Department of Chemical Research Support, Weizmann Institute of Science, Rehovot 76100, Israel

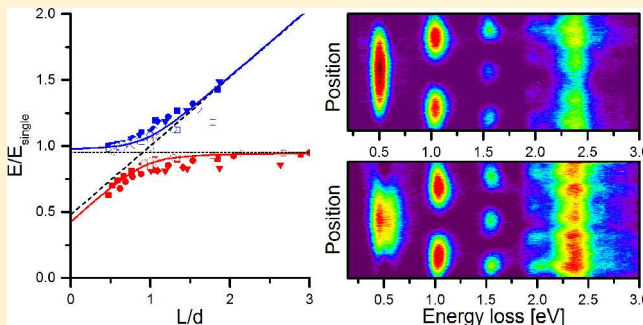
[⊥]Humboldt-Universität zu Berlin, Institut für Physik AG Theoretische Optik und Photonik, 12489 Berlin, Germany

[#]Max-Born-Institut, 12489 Berlin, Germany

Supporting Information

ABSTRACT: Electron energy loss spectroscopy (EELS) in a monochromated transmission electron microscope is applied to probe standing-wave-like cavity modes hybridized with surface plasmon polaritons (SPP) in rectangular submicron slits in a thin gold film. Coupling of hybridized SPP-cavity modes between two adjacent slits is studied by systematically varying the width of the metal bar d that separates the identical slits in a two-slit system. Measurements on two-slit systems with different slit lengths L and fixed width reveal energy shifts and mode splitting of the fundamental SPP cavity mode which can be generally described as a function of a dimensionless scaling parameter L/d . Numerical simulations with the Discontinuous Galerkin Time-Domain (DGTD) method confirm the experimental data and reveal insights into the underlying complex coupling mechanisms.

KEYWORDS: STEM EELS, surface plasmon polaritons, extraordinary optical transmission, plasmonics



Surface plasmon polaritons (SPPs) resulting from the strong interaction of light and surface plasmons play a dominant role in the miniaturization of metallic photonic devices^{1,2} and are hence of great interest.^{3,4} Most studies on plasmonic effects in metallic nanostructures were up to now performed with light-optical techniques which, despite of considerable recent progress,⁵ lack the spatial resolution to fully probe the nanoscale behavior of the involved SPPs. In contrast, in the scanning transmission electron microscopy (STEM) mode, the focused electron beam of an electron microscope is able to excite SPPs on the nanometer scale. Detection of SPPs is facilitated by electron energy loss spectroscopy⁶ which makes the combination of the two techniques (STEM EELS) a viable experimental tool in plasmonics.⁷ STEM EELS was already frequently applied to study, for example, localized surface plasmon resonances of metallic nanoparticles^{8–11} or the coupling of split-ring resonators in metamaterials.¹²

Of enormous interest in the field of plasmonics is the phenomenon of extraordinary optical transmission through subwavelength holes,^{13–15} which has been intensively studied by light-optical techniques. The application of electron microscopy combined with EELS is challenging regarding instrumental energy resolution and data processing due to the

detection limit for low-energy signals. Weak plasmonic excitations are masked by the extended tail of the zero-loss peak (ZLP) of unscattered and elastically scattered electrons in EELS spectra. An electron monochromator can significantly improve the energy resolution, defined as the full width at half-maximum (fwhm) of the ZLP, to below 0.2 eV. Most importantly, this reduces the intensity of the ZLP tail in the energy-loss range of interest^{16,17} by orders of magnitude and thus enables the analysis of low-energy SPPs. Additionally, elaborate acquisition techniques such as binned-gain averaging¹⁸ and numerical sharpening of spectra by deconvolution with the ZLP, for example, using the Richardson–Lucy algorithm,^{19,20} were shown to improve the accessible energy-loss range in STEM EELS and to detect signals with energy losses as low as 0.17 eV.²¹

Previous investigations of the plasmonic response of submicron apertures in thin metal films were performed by several groups. Particularly interesting are studies of the interaction between two and more apertures because they

Received: January 20, 2016

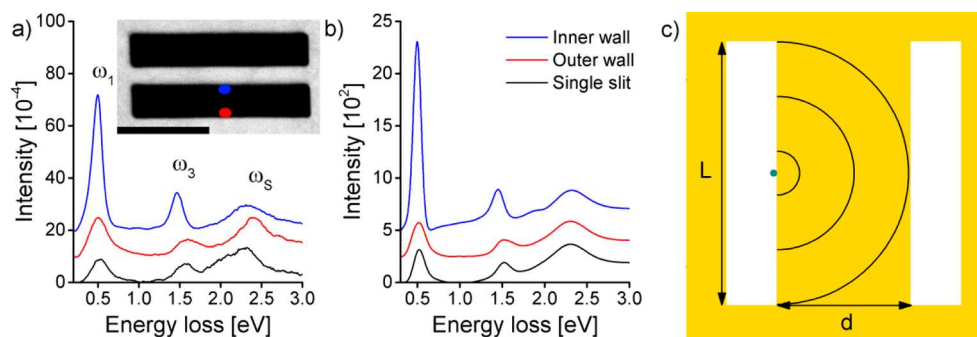


Figure 1. (a) Experimental and (b) simulated EELS spectra taken at $L/2$ at 10 nm distance to the wall in a single slit (black spectrum) and near the outer and inner walls (red and blue spectra) in a two-slit system with a length of $L = 960$ nm and a metal bar width of $d = 100$ nm. (c) Schematic of the analyzed structure. The electron beam is marked with the green dot and the coupling-mediating SPP is indicated by a circular wave. The inset in (a) shows a HAADF STEM image with red and blue dots marking the positions where the spectra were taken. The dark scale bar corresponds to 500 nm.

provide valuable information on the interaction mechanisms between electromagnetic radiation and subwavelength apertures. Alaverdyan et al.²² studied chains of nanoholes with different interhole distances by inverted dark-field microscopy. If a hole pair or a chain of eight nanoholes is illuminated in phase (wave vector of the incident light perpendicular to the chain axis, polarization parallel to the chain axis), a red-shift of the emitted light was observed for increasing hole distance. Upon further increase of the distance, a second blue-shifted mode emerges. The second mode also is red-shifted with further enlargement of the interhole distance. Eventually, light emission with a wavelength similar to the one for small hole distances is observed. Sigle et al.^{23,24} studied the plasmonic response of arrays of circular nanoholes in a thin Ag film. Ögüt et al.²⁵ revealed Fabry–Perot-like SPP resonances in individual rectangular single slits and two-slit systems by energy-filtered transmission electron microscopy (EFTEM). In two closely spaced slits, these SPP resonances were shown to hybridize due to magnetic coupling in accordance to Babinet’s principle. Via STEM EELS, Carmeli et al.²⁶ demonstrated the excitation of SPPs up to several 100 nm away from the metal wall of a single rectangular slit in a 200 nm thin Au film and showed the hybridization of SPPs with cavity modes. Prangma et al.²⁷ performed cathodoluminescence measurements in single slits and arrays of subwavelength slits in a scanning electron microscope. They investigated single slits and three-slit arrays of 100 nm x 260 nm size with varying interslit distances of 240, 300, and 350 nm. In a single slit, the fundamental cavity mode was observed at a wavelength of 680 nm. Inside the arrays (measuring close to a wall in the central slit), the observed wavelengths were 610, 640, and 670 nm and are thus all blue-shifted compared to the single slit. The blue-shift decreases for increasing the interslit distance. Zhao et al.²⁸ analyzed two-slit structures in a Ag film by finite-difference time-domain simulations assuming white-light illumination in TM polarization. By varying the interslit distance, they were able to distinguish three different coupling regimes. For short interslit distances < 50 nm, the SPP modes are coupled electrostatically, similar to dipole-coupling. For intermediate interslit distances of 50–200 nm, they supposed that the coupling is mediated by interference of SPP fields leaking through the wall between both slits. For larger interslit distances, the SPP fields inside both slits can no longer interact directly and interaction between both slits is only mediated by SPPs propagating on the film surface between both slits. In a earlier publication,²⁹ we

studied the effect of introducing a second slit by STEM EELS and found a strong enhancement of the hybridized SPP-cavity mode due to coupling to the neighboring slit. Time-domain simulations in real space elucidated the mechanism of coupling between the slits. SPPs, launched by the cavity modes, propagate at the top and bottom surfaces of the film. These SPPs excite SPP-cavity modes in the neighboring slit giving rise to back-propagating SPPs. The resulting mode intensities as a function of the slit distance can be understood by coherent interference of the originally excited and back-propagating SPPs from the neighboring slit. The time-domain simulations also revealed the occurrence of symmetric (high-energy) and antisymmetric (low-energy) SPPs (with electrical field component E_y parallel to the film surface and perpendicular to the long slit wall) propagating between two slits on the surfaces of a thin Au film. The simulations showed predominant excitation of the antisymmetric mode for small d values with the beam positioned close to the metal bar at $L/2$ (L : slit length). For a metal bar width $d = L$, simulations yielded excitation of both the symmetric and antisymmetric mode.

In this work, we aim at a deeper understanding of the excitation and coupling of SPPs in two-slit systems and how these characteristics can be influenced by the geometrical properties of the two-slit systems. For this purpose, we study two-slit systems with different slit lengths L and various metal bar widths d between the slits by STEM EELS and numerical simulations by the Discontinuous Galerkin Time-Domain (DGTD) method. The influence of SPP reflections between the two slits on the fundamental SPP-cavity mode is shown to be strongly dependent on the distance between the slits. By investigating two-slit systems with different slit lengths, our study reveals for the first time energy shifts and mode splitting of the fundamental SPP-cavity mode as a function of a dimensionless scaling parameter, namely, L/d . The analyzed SPP-cavity modes are the result of the hybridization of the resonant electromagnetic standing wave in the slit and SPPs supported on the side walls of the slits.

RESULTS AND DISCUSSION

Figure 1a shows EELS spectra acquired close to the wall of a single slit and two-slit system with $L = 960$ nm. The high-angle annular dark-field (HAADF) STEM image in Figure 1a shows the two-slit system with the positions marked by dots where EELS spectra were acquired. The basic features in all spectra are the fundamental mode (at ~ 0.5 eV denoted by ω_1) and the

third harmonic (at ~ 1.5 eV denoted by ω_3) of a standing-wave-like cavity mode along the long slit axis, which is hybridized with localized SPP resonances supported by the metal walls of the slit. The second harmonic is missing because a node is expected for this mode if spectra are taken at $L/2$. Additionally, the Au surface plasmon of the film at about 2.3 eV (denoted by ω_s) is observed in the spectrum. The spatial distributions of these basic features are shown in Figure 3a and their charge distributions are presented in Figure S1 in the Supporting Information. The intensities of the fundamental and third harmonic are enhanced by factors of 5.9 and 2.0 in the spectrum taken close to the metal bar of a two-slit system (blue spectrum in Figure 1a) compared to the spectrum of the single slit (black spectrum in Figure 1a). Moreover, the signal energies shift which is particularly obvious for the third harmonic. The changes of energies and intensities in the spectra of the two-slit system relative to the single slit clearly reflect the effects of coupling between the two slits which is mediated by the connecting metal bar. Simulations of EELS spectra by the DGTD technique are presented in Figure 1b for a single slit and a two-slit system with the same dimensions assuming the same electron beam position as in the experiments.

The energies of ω_1 , ω_3 , and surface plasmon ω_s from Figure 1 are summarized in Table 1 for the experimental and simulated

Table 1. Experimental (Left Sub-Columns) and Simulated (Right Sub-Columns) Energies of Cavity Modes and Surface Plasmon in a Single Slit and a Two-Slit System

	ω_1 (eV)		ω_3 (eV)		ω_s (eV)	
	exp	sim	exp	sim	exp	sim
single slit	0.53	0.52	1.58	1.52	2.26	2.31
double slit, outer wall	0.51	0.51	1.63	1.52	2.41	2.3
double slit, inner wall	0.49	0.50	1.47	1.45	2.35	2.32

data. The simulated energies of the fundamental mode agree well with the experimental data which demonstrates the validity of the simulation approach. Slight discrepancies are observed for the third harmonic in the single slit between simulated (1.52 eV) and experimental data (1.58 eV) and at the outer wall of the two-slit system for the third harmonic (1.63 eV experimental vs 1.52 eV simulation) and surface plasmon energies (2.41 experimental vs 2.3 eV simulation). We note that signal shifts, especially of the surface plasmon, can be induced by experimental factors, like carbon contamination of the Au film in the microscope.

The fundamental mode has a small shoulder at 0.65 eV in the experiment and simulation which can be understood by the work of Ögüt et al.²⁵ They reported two possible states (symmetric and antisymmetric) per mode order in a single slit due to weak hybridization of SPPs supported on either wall of the slit. As one of the modes is weakly excited it was only observed in their simulated data and not in the experiments. The shoulder at 0.65 eV in our experimental and simulated spectra of the single slit is attributed to the hybridization of the fundamental mode in a single slit. However, similar to the simulations of Ögüt et al.,²⁵ one of the two possible hybridized modes is only weakly excited. Henceforth, we will only focus on the strongly excited single-slit mode and for the sake of simplicity denote it the single-slit mode.

The scheme of a two-slit structure in Figure 1c visualizes the coupling between the two slits via propagating SPPs on the metal bar surfaces between the slits. The propagating SPP is

shown in a simplified way by concentric circles originating at an electron beam position of $L/2$. We emphasize that the signals $\omega_{1,3}$ in our EELS spectra are not related to the coupling-mediated SPPs on the top and bottom surfaces of the metal bar. The analyzed signals rather correspond to SPP-cavity modes which are the result of the hybridization of the resonant electromagnetic standing wave in the slit and SPPs supported on the side walls of the slits.

Figure 1 highlights the site-selective excitation of SPP-cavity modes by STEM EELS. Only odd modes are excited if the beam is positioned at $L/2$. An electron beam position close to the central metal bar excites coupled modes which are strongly affected by the presence of the second slit. Positioning the beam near the outer wall yields mode intensities which are not or only weakly affected by interslit coupling.

In the following, we focus on the fundamental mode because it is influenced most significantly upon introduction of a neighboring slit and shows the strongest intensity enhancement compared to the other harmonics in two-slit systems. Moreover, the fundamental mode is expected to be most relevant for effects concerning light emission from these structures. To further investigate coupling effects between the two slits, two-slit systems with $L = 960$ nm and varying metal bar widths $d = 100, 270, 720, 900,$ and 1800 nm were prepared. Figure 2 shows experimental spectra of the fundamental mode at the outer wall (Figure 2a), the inner wall (Figure 2b), and simulated spectra at the outer and inner wall (Figure 2c,d), respectively. At first sight, the experimental spectra at the outer wall in the two-slit systems appear to be all quite similar to the single-slit spectrum (black spectrum in Figure 2a).

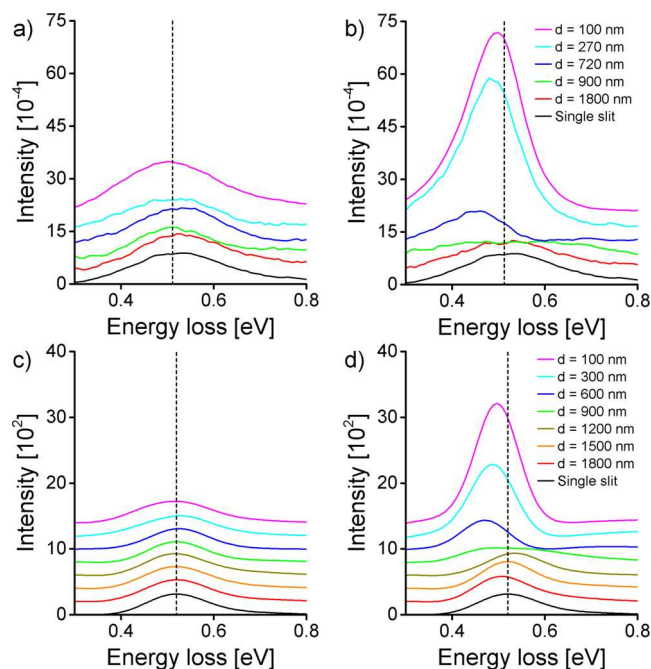


Figure 2. Experimental EELS spectra taken at $L/2$ and 10 nm distance from (a) the outer and (b) the inner walls of a two-slit system with $L = 960$ nm and varying metal bar widths d . (c, d) Simulated EELS spectra for different d values calculated for the corresponding experimental conditions at the outer and inner walls. A spectrum taken in a single slit at the corresponding positions is included in each subfigure for reference. In addition, the fundamental energy of the single slit is marked by a dashed line.

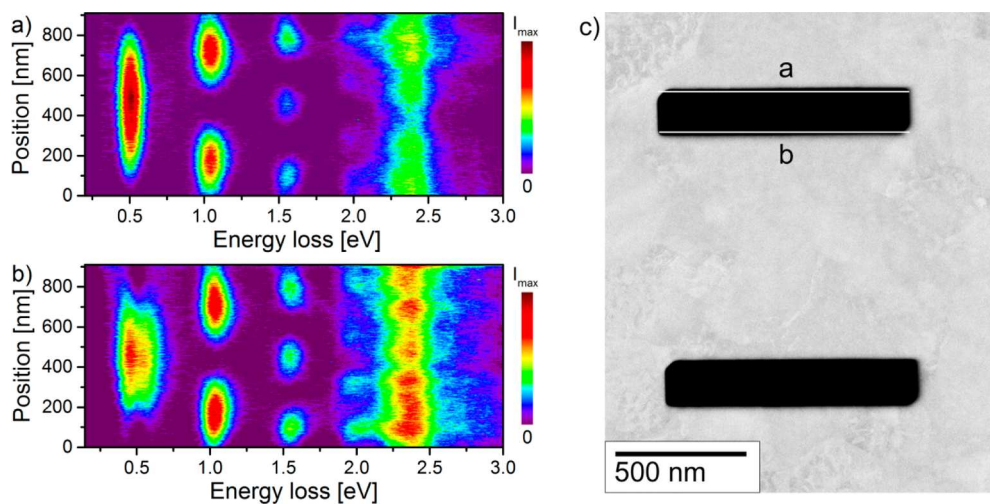


Figure 3. Measured EELS intensity along the long slit wall at the (a) outer and (b) inner wall of a two-slit system with $L = 960$ nm and $d = 900$ nm. The intensity scaling is identical in (a) and (b). (c) HAADF STEM image of the two-slit system with white lines and letters a and b referring to the linescan positions of the spectra presented in (a) and (b).

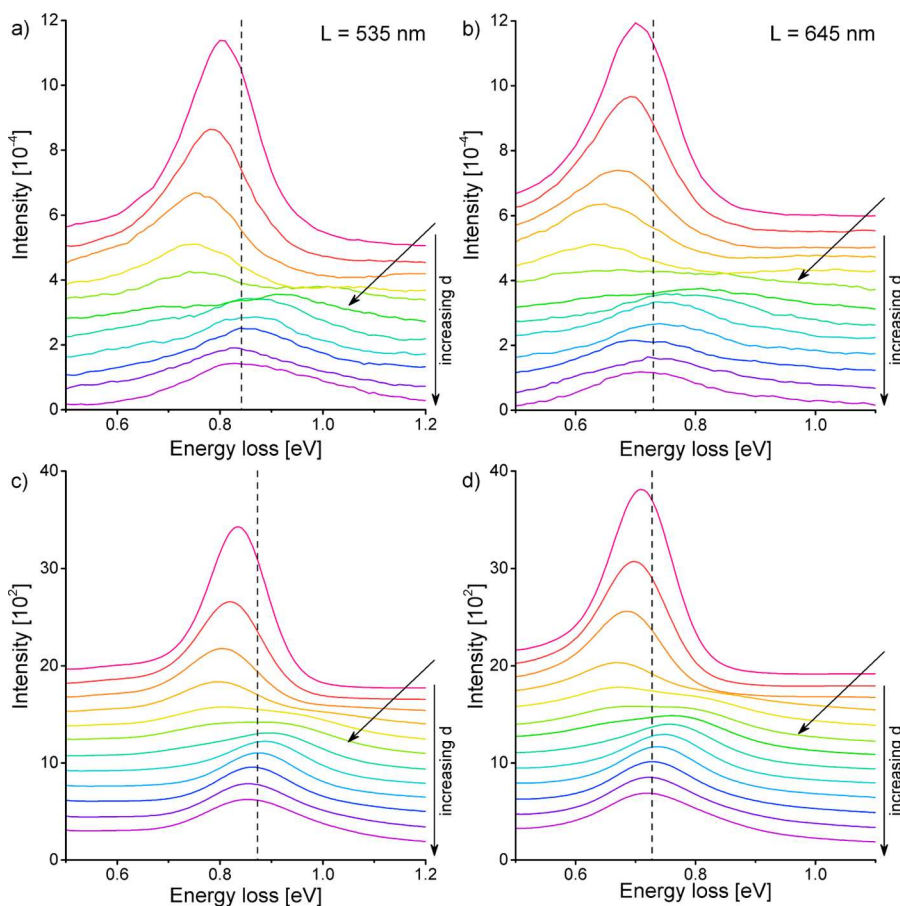


Figure 4. (a, b) Experimental EELS data obtained at the inner wall in a two-slit system with (a) $L = 535$ and (b) 645 nm. The slit distance is systematically varied from ~ 100 nm (uppermost spectrum) to $\sim 2L$ (bottom spectrum). The spectra corresponding to $d = L$ are marked with an arrow. (c, d) Simulated EELS spectra. The energy of the fundamental mode in a single slit of identical length is indicated by the vertical dashed line in each subfigure.

Close to the inner wall (Figure 2b), however, the individual spectra for ω_1 differ significantly as far as energy and intensity are concerned. With increasing slit distance from 100 to 720 nm, the energy of the fundamental mode gradually shifts toward lower values. Particularly striking is the strong intensity

reduction at $d = 900$ nm and the appearance of a very broad peak hinting at a splitting of the fundamental mode into two modes (green spectrum in Figure 2b). In the case of $d = 1800$ nm, the fundamental mode appears as a single peak at 0.52 eV, similar to the energy at small d and the energy in the single slit.

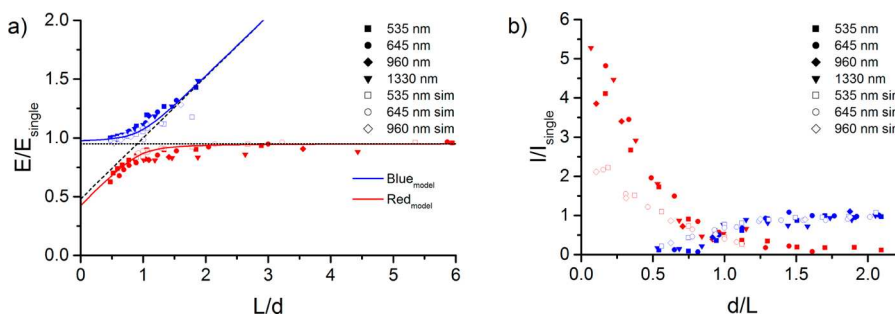


Figure 5. (a) Experimental and simulated energies of the red- and blue-shifted fundamental mode (normalized with respect to the single-slit energy) plotted as a function of L/d . The dotted and dashed lines correspond to \tilde{E}_0 and \tilde{E}_1 derived from a phenomenological model (cf. text). (b) Experimental and simulated intensity of the fundamental mode (normalized with respect to the single-slit intensity) plotted against d/L . Squares, circles, diamonds, and triangles correspond to slit lengths of $L = 535, 645, 960,$ and 1330 nm. Full and empty symbols represent experimental and simulated data. The data of the red-shifted and blue-shifted mode is color-coded in red and blue.

Figure 2c,d depicts calculated EELS spectra of the fundamental mode for comparison with the experimental data in Figure 2a,b. The simulated spectra clearly confirm the observed energy shifts and splitting of the fundamental cavity resonance with increasing d . At $d = 900$ nm, the fundamental mode also appears as a broad peak. As a side note, if the simulated spectrum is not convoluted with a Gaussian function to account for the finite energy resolution in the experiments, the fundamental mode appears clearly split. At $d = 1200$ nm, the fundamental mode is clearly shifted toward higher energy compared to the single slit and the peak width is further reduced.

The assumed two weak signals located inside the broad peak associated with the fundamental mode at $d = 900$ nm are difficult to detect in the experiments performed in the FEI Titan (cf. Figure 2b) due to the limited energy resolution. We therefore performed experiments in the ZEISS SESAM microscope with superior energy resolution. Figure 3a,b shows the color-coded EELS intensity along the long slit wall acquired close to the outer and inner wall in a two-slit system with $L = 960$ nm and $d = 900$ nm. The positions of the EELS line profiles are marked by white lines in the HAADF STEM image of the two-slit structure in Figure 2c. The expected Fabry–Perot pattern of the cavity modes ω_1 to ω_4 can be well recognized and so can the surface plasmon peak of gold at ~ 2.4 eV. The higher modes ω_2 to ω_4 only show slight intensity enhancements near the inner wall (the color scales are identical in Figures 3a,b) and do not shift in energy. The fundamental mode ω_1 , however, is significantly different at the two slit walls. At the outer wall it is located at 0.51 eV, whereas it is clearly split at the inner wall into two peaks at 0.46 and 0.58 eV. The splitting also leads to a reduced intensity of the fundamental mode, similar to the green spectra in Figures 2b,d.

Figure 4a,b show spectra obtained close to the inner wall in two-slit systems with $L = 535$ and 645 nm with systematically varied distances between the slits from ~ 100 nm to $2L$. Shorter slit lengths were chosen to visualize more clearly the effect of coupling because ω_1 exhibits a higher energy that can be more easily extracted from the tail of the ZLP. Increasing interslit distances result in a gradual shift of the fundamental mode toward lower energy. The spectrum for $d = L$ (lime green spectrum marked by an arrow in Figure 4a) shows two weak peaks. The lower-energy mode vanishes with further increasing d , whereas the higher-energy peak shifts toward lower energies (spectra marked in green and blue colors). At $d = 2L$, the former higher-energy peak coincides with the single-slit energy

(marked by the vertical dashed line) of the fundamental mode (purple spectrum in Figure 4a). The same behavior is observed in Figure 4b for a slit length of 645 nm. At $d = L$ (lime green spectrum marked by an arrow in Figure 4b), however, only a single broad peak rather than two distinct ones is discernible. Figure 4c,d show simulated EELS spectra corresponding to the experimental ones depicted in Figure 4a,b. The behavior of the simulations qualitatively agrees with the experimental data. The absolute energies, however, differ from the experimental ones. For $L = 535$ nm (Figure 4c), the simulated single slit energy is larger than in the experiments.

Figure 5a summarizes the observed energy shifts of ω_1 with respect to the single-slit energy for all slit lengths plotted as a function of L/d , a dimensionless scaling parameter. Squares, circles, diamonds, and triangles correspond to slit lengths of $L = 535, 645, 960,$ and 1330 nm. Full and empty symbols represent experimental and simulated data, respectively. In the following, we denote the mode with energies below that of the single slit (red data points) as red-shifted mode and the other mode (blue data points) as blue-shifted mode. The splitting of the fundamental mode can be described by two energy branches which approach asymptotically (i.e., for $L/d \gg 1$ or $\ll 1$) two intersecting straight lines given by $\tilde{E}_0 = 0.95$ and $\tilde{E}_1 = 0.5 + 0.5L/d$, where $\tilde{E}_i \equiv E_i/E_{\text{single}}$, $i = 0, 1$ and $E_{\text{single}} = \hbar c\pi/L$. Both experiment and simulation can be described well by this behavior.

To account for the experimental and simulated data presented in Figure 5a, we employ a phenomenological model, in which the two intersecting modes are considered as two, linearly coupled, harmonic oscillators.³⁰ The normalized energies, $\tilde{E}_{\text{blue/red}}$, of the two coupled branches result from the secular equation³⁰

$$\begin{vmatrix} \tilde{E}_0^2 - \tilde{E}^2 & \kappa \\ \kappa & \tilde{E}_1^2 - \tilde{E}^2 \end{vmatrix} = 0$$

with the solutions

$$\tilde{E}_{\text{blue/red}}^2 = \frac{\tilde{E}_0^2 + \tilde{E}_1^2}{2} \pm \sqrt{\left(\frac{\tilde{E}_0^2 - \tilde{E}_1^2}{2}\right)^2 + \kappa^2}$$

The best fit of the experimental data in Figure 5a is obtained for the coupling constant $\kappa = 0.193$. To properly interpret the resulting uncoupled branches, their energies $E_0 \approx \hbar ck_0$, with k_0

$= \pi/L$ and $E_1 = \hbar ck_1$, with $k_1 = \pi^{1/L+1/d}/2$, should be considered. The first uncoupled mode with an energy close to $\hbar ck_0$, is the single-slit cavity mode. The slight deviation of its energy from the expected value may be due to slight deviation of the slit lengths L in the two-slit sample as compared to the single-slit one. The second uncoupled mode, with energy $E_1 = \hbar ck_1$, is a standing SPP wave hybridized with the cavity mode of the neighboring slit. The energy of a pure standing SPP wave, arising from multiple reflection across the metal bar, would depend only on the metal bar width d , that is, $E_1 = \hbar c\pi/d$ and would go to zero at very large values of d . The intersection of \tilde{E}_1 with E/E_{single} at 0.5 is clearly inconsistent with such a pure mode. However, within our phenomenological model, this nonvanishing intersection occurs due to hybridization with the cavity mode of the neighboring slit. The effective wavenumber k_1 of the hybridized mode cannot be related, via the usual photon dispersion relation, to the norm $\pi\sqrt{(1/L)^2 + (1/d)^2}$ of the total wave vector, as would be expected under momentum conservation requirement, due to scattering at the slit edges and rims. Instead, it is determined by the (arithmetic) average of the well-defined uncoupled mode energies, which are assumed to be sufficiently close to each other (i.e., $1/L \sim 1/d$) for the precoupling hybridization scheme to be strictly valid. The apparent vanishing of the intensity of the blue-shifted branch for $d/L < 0.5$ and of the intensity of red-shifted branch for $d/L > 1.5$ shown in Figure 5b is consistent with this requirement. The slit length L in the coupled oscillator model has to be replaced with an effective length as the energy $E_{\text{single}} = \hbar c\pi/L$ is the energy of the SPP supported by a single wall and not by a single slit. In the latter case, the fundamental energy is altered due to hybridization of SPPs on either slit wall.^{25,26} The experimentally determined single-slit energy of 0.53 eV (in contrast to $E_{\text{single}} = \hbar c\pi/L = 0.65$ eV for $L = 960$ nm), therefore, corresponds to an effective slit length $L_{\text{eff}} = L + 210$ nm.

This simple phenomenological, avoided-crossing model of a cavity mode, coupled to a neighboring cavity mode via hybridization to a standing SPP wave, reproduces quite well our experimental results for the energy splitting of the fundamental cavity-mode (cf. full and empty symbols in Figure 5). The coupling, leading to the avoided level crossing, arises due to scattering of SPPs at the slit edges and rims, thus, mediating interaction between the cavity modes in the two identical slits. Without coupling, both slits form a degenerate two-slit system with identical energies of the fundamental cavity modes. However, if coupling occurs between the slits, the degeneracy is lifted due to formation of symmetric and antisymmetric combinations of the cavity modes in the two slits. Our previous real-time real-space simulations²⁹ have already revealed the occurrence of symmetric and antisymmetric SPPs propagating between two slits on the surfaces of a thin Au film.

The intensity of the two branches of the fundamental mode, normalized with respect to the single-slit intensity, is plotted as a function of d/L in Figure 5b. Interestingly, the variation of the normalized intensity of the fundamental mode is independent of the absolute distance between slits and depends only on d/L . The coupling is mediated by SPPs traveling back and forth between the two slits. In the case of the largest slit length, SPPs travel significantly longer distances as compared to the shorter slits. Hence, the intensity drop could be expected to depend

directly on the absolute interslit distance which is clearly not the case in our experiments. However, the cavity-mode wavelength increases with slit length L and the propagation distance normalized to the wavelength of the cavity mode is identical for fixed values of d/L . This fact shows the strong intertwinement of cavity modes and SPPs that mediate coupling.

It is instructive to compare the energy and intensity variations with respect to the dimensionless scaling parameter. The energy shift of the two modes in Figure 5a is almost symmetrical with respect to $L/d = 1$. Hence, the intensity distribution between the two modes should also be symmetrical if only avoided level crossing was taken into account. Therefore, another effect must be invoked to explain the strong intensity enhancement of the red-shifted mode for small interslit distances (cf. Figure 5b). Direct interaction of the electromagnetic fields of the SPPs in both slits can be ruled out as the skin depth of Au is far smaller than the metal bar width. Our previous simulations²⁹ have shown that the E_y -fields (in the film plane, perpendicular to the long slit axis) are antisymmetric for small interslit distances in both slits. These fields lead to the accumulation of identical charges on both walls of the metal as also shown by the simulations by Ögüt et al.²⁵ As a side note, the system is dynamic and the “static” description by charge accumulation is only valid for short time intervals. In reality, the electric fields and charges (in form of SPPs supported by the slit walls) oscillate. If the metal bar is narrow enough for constructive interference of the SPPs (i.e., summation of identical charges) on either side of the bar, the experimentally observed strong intensity enhancement for the red-shifted mode occurs (cf. Figure 5b for $d/L < 0.6$). If the interslit distance increases, the SPPs on either side of the metal bar cannot interfere with each other and intensity enhancements are not observed anymore. Figure 5b shows that the simulated intensities are significantly smaller for $d/L < 0.5$, whereas a good agreement is observed for larger d/L . As mentioned above, for small interslit distances the interaction of SPPs on either side of the metal bar governs the intensity. This interaction must be weaker in the simulations to explain the reduced intensities. Deviations from the ideal rectangular slit geometry in the experiments could be the origin of this effect. In the simulation, the slits have well-defined sharp edges whereas the experimental slit structures have rounded edges due to limitations of the FIB preparation. Intuitively one would expect the imperfect geometry to give reduced intensities but here it is reversed. Scattering at the sharp edges constitutes a loss channel for SPPs by photon emission,³¹ leading to smaller intensities in the simulations at small d/L .

In the following, we discuss our results with respect to light-optical studies. The categorization of coupling phenomena into different regimes was also proposed by Zhao et al.²⁸ The first coupling regime proposed with $d < 50$ nm cannot be observed in our experiments. The second coupling regime corresponds to our experimentally observed strong intensity enhancement of the red-shifted mode. By taking into account these different coupling regimes, the asymmetric intensity variation for the red-shifted and blue-shifted modes in our experiments (cf. Figure 5b) can be explained. However, such a comparison is not feasible for our observed energy shifts. Zhao et al. used two-slit systems with different widths for each slit and hence their fundamental energies differ inherently. The coupling of two nonidentical slits is more complex because each slit eigenmode is subject to energy shifts and splitting.

Mode splitting similar to our experimental data from Figure 5a was also observed in light-optical experiments by Alarverdyan et al.²² The behavior of the energy shifts of the emitted light closely resembles the energy shifts of the SPP-cavity modes in our STEM EELS experiments. We have shown that the coupling phenomena can be well described by a dimensionless scaling parameter, that is, the slit length normalized with respect to the interslit distance. The coupling is mediated by SPPs propagating on the film surface. These SPPs are also responsible for the far-field light emission due to scattering at the slit edges. The occurrence of the mode splitting in both EELS (sensitive to the cavity modes E_z -field component along the electron beam direction) and far-field emission (related to SPPs on the film surface) shows the strong interaction of cavity modes and coupling-mediating SPPs.

The cathodoluminescence measurements performed by Prangma et al.²⁷ can be treated similar to our dimensionless scaling parameter approach and lead to L/d of 1.09, 0.87, and 0.75. Following our line of argumentation, for this range of the dimensionless scaling parameter, both modes should be present although the antisymmetric lower-energy mode would be only weakly excited. This expectation is confirmed by their data. Even a quantitative comparison to our data is possible because the relative blue-shifts in their experiments (10, 6, and 1%) for the different values of the dimensionless scaling parameter are similar as in our data.

SUMMARY

We have used STEM EELS measurements and DGTD simulations to investigate the coupling of hybridized SSP cavity modes in rectangular submicron slits with a fixed width of 180 nm with respect to variations of the slit length L and the interslit distance d . The unperturbed single-slit fundamental mode hybridizes in two-slit systems into an antisymmetric, red-shifted mode and a symmetric, blue-shifted mode in analogy to an avoided level crossing of two coupled oscillators. The behavior of the fundamental mode was analyzed in detail by studying the energy shifts and mode intensities as a function of the slit length L and width d of the metal bar between the slits. The energy shifts and intensities of the red- and blue-shifted modes can be generally described by a dimensionless scaling parameter L/d , independent of the individual slit lengths. The energies of the blue- and red-shifted modes are significantly shifted compared to the single-slit energy. The spectral behavior is symmetric with respect to $L/d = 1$. However, the mode intensities differ significantly from a symmetric behavior: The red-shifted mode is strongly enhanced for large values of L/d (i.e., small distance between slits), whereas the blue-shifted mode dominates for $L/d < 1$. The enhancement of the red-shifted mode can be understood by constructive interference of the SPPs on both sides of the metal bar separating the slits (see Supporting Information). These findings are confirmed quantitatively by numerical simulations. The ability to alter the SPP wavelength and intensity by changing the slit length and/or the interslit distance allows to tailor the SPP parameters to match the requirements of possible technological applications, for example, in plasmonic circuits.

METHODS

The thin Au film was prepared by evaporation of 200 nm Au on a mica substrate which was pretreated by a thin layer of dish-washing detergent to facilitate floating off and transfer onto Cu

TEM grids. Without the detergent treatment, the Au films adhere strongly to the mica and cannot be floated off. Folding grids were employed to enhance specimen stability due to weak adhesion of the Au film to the grid. Single and double rectangular slits with lengths of 535, 645, 960, and 1330 nm and a width of 180 nm were prepared by focused-ion-beam (FIB) milling in an FEI DualBeam STRATA 400S. To study the coupling between the two slits, the distance between the slits was varied from 100 nm up to $2L$.

An FEI Titan³ 80–300 operated at 300 kV was used for STEM EELS. The instrument is equipped with a Wien-type filter monochromator and a Gatan Tridiem 865 HR imaging filter. Under monochromated conditions, the achievable energy and spatial resolutions are 0.12 eV and ~ 1 nm, respectively. For each measurement, 50 spectra with a dwell time of 10 ms were acquired with the binned-gain averaging method¹⁸ and summed up after energy drift correction. The Richardson–Lucy algorithm^{19,20} was applied for sharpening the EELS spectra. A vacuum spectrum obtained without an inserted specimen was used as point spread function for deconvolution. Seven iterations of the Richardson–Lucy algorithm were applied to the acquired spectra, leading to a significant improvement of the energy resolution. Typically, the fwhm of the ZLP was reduced from 110 to 70 meV. After spectral sharpening, background subtraction was performed by fitting a biexponential curve to the right shoulder of the ZLP. Two different exponents are necessary to accurately model the change of slope from the sharply falling edge to the extended tail. The RL deconvolution has to be used to be able to resolve the relevant peaks in the tail of the ZLP and to reveal mode splitting. As quantification of signals may be altered by RL deconvolution, various tests were performed. Detrimental effects on the spectra can be ruled out after these tests for the relevant energy-loss range and the number of iterations applied ($n = 7$). The reader is referred to the Supporting Information for details. All spectra were taken at $L/2$ with 10 nm distance to the respective slit walls.

Additional measurements (Figure 3) were performed in a ZEISS SESAM microscope at 200 kV. The instrument is equipped with an Omega-type monochromator and a MANDOLINE energy filter which yield an energy resolution of 74 meV.^{17,32}

Numerical simulations were carried out by the Discontinuous Galerkin Time-Domain (DGTD) method³³ with the necessary adaptations to calculate EELS spectra.³⁴ The only difference is the use of a pure scattered field formalism to directly access the field induced by the electron. The permittivity of Au in the whole energy range was modeled by fitting a single Drude and 3 Lorentz terms to the experimental data from Johnson and Christy.³⁵ The lateral film size was finite with a size of at least $3 \times 3 \mu\text{m}^2$ to reduce artifacts from the edges. It is surrounded by air and perfectly matched layers to suppress reflections from the boundary of the computational domain. To accurately resolve the incident field of the electron, third-order elements with element sizes down to 10 nm were employed. The simulated data was convoluted with a Gaussian function of 100 meV full width at half-maximum to take into account the finite energy resolution in the experiments.

■ ASSOCIATED CONTENT

● Supporting Information

The Supporting Information is available free of charge on the ACS Publications website at DOI: 10.1021/acsp Photonics.6b00045.

Charge distributions of the various SPP cavity modes and their hybridization. Deconvolution with the Richardson-Lucy algorithm and evaluation of its performance for quantification of signals (PDF).

■ AUTHOR INFORMATION

Corresponding Author

* E-mail: roman.walther@kit.edu.

Notes

The authors declare no competing financial interest.

■ ACKNOWLEDGMENTS

This research was supported by a cooperation grant of the Karlsruhe Institute of Technology's Center for Functional Nanostructures (CFN), the Weizmann Institute Nano Initiative (WINI), and the Technion Russell Berrie Nanotechnology Institute (RBNI) and by the Weizmann's Helen and Martin Kimmel Center for Nanoscale Science (H.C.). K.B. and C.M. acknowledge support by the Deutsche Forschungsgemeinschaft (DFG) through Project Bu 1107/7-2. The research leading to these results received funding from the European Union Seventh Framework Program [FP/2007/2013] under Grant Agreement No. 312483 (ESTEEM2).

■ REFERENCES

- (1) Barnes, W. L.; Dereux, A.; Ebbesen, T. W. Surface plasmon subwavelength optics. *Nature* **2003**, *424*, 824–830.
- (2) Zayats, A. V.; Smolyaninov, I. I.; Maradudin, A. A. Nano-optics of surface plasmon polaritons. *Phys. Rep.* **2005**, *408*, 131–314.
- (3) Gramotnev, D. K.; Bozhevolnyi, S. I. Plasmonics beyond the diffraction limit. *Nat. Photonics* **2010**, *4*, 83–91.
- (4) MacDonald, K. F.; Samson, Z. L.; Stockman, M. I.; Zheludev, N. I. Ultrafast active plasmonics. *Nat. Photonics* **2009**, *3*, 55–58.
- (5) Schnell, M.; Garcia Etxarri, A.; Huber, A. J.; Crozier, K.; Aizpurua, J.; Hillenbrand, R. Controlling the near-field oscillations of loaded plasmonic nanoantennas. *Nat. Photonics* **2009**, *3*, 287–291.
- (6) Raether, H. Surface Plasma Oscillations as a Tool for Surface Examinations. *Surf. Sci.* **1967**, *8*, 233–246.
- (7) Garcia de Abajo, F. J. Optical excitations in electron microscopy. *Rev. Mod. Phys.* **2010**, *82*, 209–275.
- (8) Cohen, H.; Maniv, T.; Tenne, R.; Hacoheh, Y. R.; Stephan, O.; Colliex, C. Near-field electron energy loss spectroscopy of nanoparticles. *Phys. Rev. Lett.* **1998**, *80*, 782–785.
- (9) Nelayah, J.; Kociak, M.; Stephan, O.; de Abajo, F. J. G.; Tence, M.; Henrard, L.; Taverna, D.; Pastoriza-Santos, I.; Liz-Marzan, L. M.; Colliex, C. Mapping surface plasmons on a single metallic nanoparticle. *Nat. Phys.* **2007**, *3*, 348–353.
- (10) Bosman, M.; Keast, V. J.; Watanabe, M.; Maarroof, A. I.; Cortie, M. B. Mapping surface plasmons at the nanometre scale with an electron beam. *Nanotechnology* **2007**, *18*, 165505–5.
- (11) Pelton, M.; Aizpurua, J.; Bryant, G. Metal-nanoparticle plasmonics. *Laser Photonics Rev.* **2008**, *2*, 136–159.
- (12) von Cube, F.; Irsen, S.; Diehl, R.; Niegemann, J.; Busch, K.; Linden, S. From Isolated Metaatoms to Photonic Metamaterials: Evolution of the Plasmonic Near-Field. *Nano Lett.* **2013**, *13*, 703–708.
- (13) Genet, C.; Ebbesen, T. W. Light in tiny holes. *Nature* **2007**, *445*, 39–46.
- (14) Garcia-Vidal, F. J.; Martin-Moreno, L.; Ebbesen, T. W.; Kuipers, L. Light passing through subwavelength apertures. *Rev. Mod. Phys.* **2010**, *82*, 729–787.
- (15) Ebbesen, T. W.; Lezec, H. J.; Ghaemi, H. F.; Thio, T.; Wolff, P. A. Extraordinary optical transmission through sub-wavelength hole arrays. *Nature* **1998**, *391*, 667–669.
- (16) Terauchi, M.; Tanaka, M.; Tsuno, K.; Ishida, M. Development of a high energy resolution electron energy-loss spectroscopy microscope. *J. Microsc.* **1999**, *194*, 203–209.
- (17) Koch, C. T.; Sigle, W.; Höschen, R.; Rühle, M.; Essers, E.; Benner, G.; Matijevic, M. SESAM: Exploring the Frontiers of Electron Microscopy. *Microsc. Microanal.* **2006**, *12*, 506–514.
- (18) Bosman, M.; Keast, V. J. Optimizing EELS acquisition. *Ultramicroscopy* **2008**, *108*, 837–46.
- (19) Zuo, J. M. Electron detection characteristics of a slow-scan CCD camera, imaging plates and film, and electron image restoration. *Microsc. Res. Tech.* **2000**, *49*, 245–68.
- (20) Gloter, A.; Douiri, A.; Tence, M.; Colliex, C. Improving energy resolution of EELS spectra: an alternative to the monochromator solution. *Ultramicroscopy* **2003**, *96*, 385–400.
- (21) Rossouw, D.; Botton, G. A. Plasmonic Response of Bent Silver Nanowires for Nanophotonic Subwavelength Waveguiding. *Phys. Rev. Lett.* **2013**, *110*, 066801–5.
- (22) Alaverdyan, Y.; Sepulveda, B.; Eurenus, L.; Olsson, E.; Kall, M. Optical antennas based on coupled nanoholes in thin metal films. *Nat. Phys.* **2007**, *3*, 884–889.
- (23) Sigle, W.; Nelayah, J.; Koch, C. T.; van Aken, P. A. Electron energy losses in Ag nanoholes from localized surface plasmon resonances to rings of fire. *Opt. Lett.* **2009**, *34*, 2150–2152.
- (24) Sigle, W.; Nelayah, J.; Koch, C. T.; Ogut, B.; Gu, L.; van Aken, P. A. EFTEM study of surface plasmon resonances in silver nanoholes. *Ultramicroscopy* **2010**, *110*, 1094–1100.
- (25) Ögüt, B.; Vogelgesang, R.; Sigle, W.; Talebi, N.; Koch, C. T.; van Aken, P. A. Hybridized metal slit eigenmodes as an illustration of Babinet's principle. *ACS Nano* **2011**, *5*, 6701–6.
- (26) Carmeli, I.; Itskovskiy, M. A.; Kauffmann, Y.; Shaked, Y.; Richter, S.; Maniv, T.; Cohen, H. Far- and near-field electron beam detection of hybrid cavity-plasmonic modes in gold microholes. *Phys. Rev. B: Condens. Matter Mater. Phys.* **2012**, *85*, 041405–5.
- (27) Prangma, J. C.; van Oosten, D.; Kuipers, L. Local investigation of the optical properties of subwavelength rectangular holes with a focused beam of electrons. *Philos. Trans. R. Soc., A* **2011**, *369*, 3456–3471.
- (28) Zhao, B.; Yang, J.; Min, C.; Yuan, X. *Plasmonics* **2015**, *10*, 1275.
- (29) Walther, R.; Carmeli, I.; Schneider, R.; Gerthsen, D.; Busch, K.; Matyssek, C.; Shvarzman, A.; Maniv, T.; Richter, S.; Cohen, H. Interslit Coupling via Ultrafast Dynamics across Gold-Film Hole Arrays. *J. Phys. Chem. C* **2014**, *118*, 11043–11049.
- (30) Slater, J. C.; Frank, N. F. *Introduction to Theoretical Physics*; McGraw-Hill Book Company: New York, 1933; pp 107–108.
- (31) Maier, S. A. *Plasmonics: Fundamentals and Applications*; Springer Science LLC: New York, 2007.
- (32) Essers, E.; Benner, G.; Mandler, T.; Meyer, S.; Mittmann, D.; Schnell, M.; Höschen, R. Energy resolution of an Omega-type monochromator and imaging properties of the MANDOLINE filter. *Ultramicroscopy* **2010**, *110*, 971–980.
- (33) Busch, K.; König, M.; Niegemann, J. Discontinuous Galerkin methods in nanophotonics. *Laser Photonics Rev.* **2011**, *5*, 773–809.
- (34) Matyssek, C.; Niegemann, J.; Hergert, W.; Busch, K. Computing electron energy loss spectra with the Discontinuous Galerkin Time-Domain method. *Photonics Nanostruct.* **2011**, *9*, 367–373.
- (35) Johnson, P. B.; Christy, R. W. Optical Constants of Noble Metals. *Phys. Rev. B* **1972**, *6*, 4370–4379.